Geophys. J. Int. (2006) **164,** 411–424 doi: 10.1111/j.1365-246X.2005.02829.x

Complete synthetic seismograms up to 2 Hz for transversely isotropic spherically symmetric media

Kenji Kawai,[1] Nozomu Takeuchi[2] and Robert J. Geller[1]

[1]*Department of Earth and Planetary Science, Graduate School of Science, Tokyo University, Hongo* 7-3-1*, Bunkyo-ku, Tokyo* 113-0033*, Japan. E-mail: kenji@eps.s.u-tokyo.ac.jp*

[2]*Earthquake Research Institute, Tokyo University, Yayoi* 1-1-1*, Bunkyo-ku, Tokyo* 113-0032*, Japan*

Accepted 2005 October 5. Received 2005 September 30; in original form 2005 April 21

SUMMARY

We use the direct solution method (DSM) with optimally accurate numerical operators to calculate complete (including both body and surface waves) three-component synthetic seismograms for transversely isotropic (TI), spherically symmetric media, up to 2 Hz. We present examples of calculations for both deep (600 km) and shallow (5 km) sources. Such synthetics should be useful in forward and inverse studies of earth structure. In order to make these calculations accurately and efficiently the vertical grid spacing, maximum angular order, and cut-off depth must be carefully and systematically chosen.

Key words: angular order, direct solution method, shallow earthquakes, synthetic seismograms, transverse isotropy, 2 Hz.

1 INTRODUCTION

The volume of high-quality broad-band digital seismic waveform data has greatly increased in recent years. The installation of broad-band seismic arrays (Rost & Thomas 2002; Rost & Garnero 2004) and ocean bottom and borehole observatories (Sutherland *et al.* 2004; Suetsugu *et al.* 2005) has also provided valuable new data. In most cases only secondary data, which are extracted from the observed waveform data (e.g. traveltimes) are used in studies of earth structure. Body-wave waveform data for shallow events are also an important data set for studies of earth structure. The development of new computational methods for further analysing waveform data is thus highly desirable.

In recent times computational technology has made great progress. Parallelized programs using inexpensive PC clusters can provide throughput comparable to supercomputers. Although high-end supercomputers are still faster than PC clusters, due to restrictions on public use it is often difficult to access supercomputers. Currently a single node of a high-performance computer (HPC) with an Intel Pentium 4, 3.2 GHz processor costs about 200 000 Yen (roughly 2000 USD). The performance of HPCs will continue to improve. It is desirable to develop seismological tools to take full advantage of their computational performance. This paper is one such effort.

Studies of the Earth's internal structure, particularly the fine structure of the upper mantle transition zone and D″, are one of the most important tools for obtaining constraints on geodynamic processes. One approach (e.g. Woodhouse & Dziewonski 1984) is to conduct direct inversion for the global earth structure. However, as a practical matter, global coverage is highly uneven, and in many cases it is useful to gather extensive profiles from a small geographic region and invert for the 1-D structure of the study region. The 3-D structure is thus studied by comparing a patchwork of 1-D structures for each of the well-sampled regions (e.g. the regions for which coverage from arrays or dense networks is available). Studies of the D″ layer (Mitchell & Helmberger 1973; Lay & Helmberger 1983; Young & Lay 1990; Kendall & Nangini 1996; Garnero & Lay 2003) and the transition zone (Tajima & Grand 1998; Shito & Shibutani 2001; Tseng & Chen 2004) are examples of this approach.

In many cases of 1-D fine structure studies important information is contained in overlapping seismic phases, such as upper mantle triplications or S and ScS for the D″ region; comparison of synthetic seismograms to observed data is a vital step in analysing the data (Lay & Helmberger 1983; Song & Helmberger 1998; Tajima & Grand 1998). Since the data are in many cases broad-band, in such cases it is necessary (or at least highly desirable) to be able to calculate synthetic seismograms up to frequencies of 1 or 2 Hz.

At present there are three main possible approaches for computing synthetic seismograms for 1-D media:

(1) superposition of normal modes (Woodhouse & Dziewonski 1984; Yu & Park 1993; Li & Romanowicz 1995; Park 1997),
(2) reflectivity (Keith & Crampin 1977; Fryer & Frazer 1987) and
(3) the direct solution method (DSM, see references below).

Due to the difficulty of computing, storing and summing a large number of overtones, it is generally considered impractical to use modal superposition at frequencies higher than about 0.15 Hz. We have not examined this question in detail, but as we are unaware of any published studies that have used modal superposition to compute full-wave (including both body and surface waves) synthetics at frequencies higher than 0.15 Hz, we do not consider modal

superposition methods further in this paper. Reflectivity methods have been used in several studies of 1-D structure (e.g. Tajima & Grand 1998; Moore *et al.* 2004) but the computations must be carried out in cylindrical coordinates, which means that an earth-flattening transformation must be used, resulting in numerical inaccuracy (Ascher 1988). Methods for directly solving the strong form of the equation of motion (Takeuchi & Saito 1972) have been given by Chapman & Phinney (1970) and Friederich & Dalkolmo (1995). Such methods are in principle equivalent to our methods for solving the weak form of the equation of motion.

Seismic tomography has greatly advanced our knowledge of the structure of the Earth's deep interior, but almost all studies to date (especially body-wave studies) have assumed isotropic models [or have used scaling relations to reduce the number of unknown elastic constants in transversely isotropic (TI) media from 5 to 2]. On the other hand, it is well known that there is significant anisotropy of seismic structure in the mantle (e.g. Montagner & Kennett 1996), and that information on the anisotropic structure is important for understanding flow and deformation processes in the Earth (e.g. Karato 1998).

Detailed comparison of observed seismic waveform data (as observed at an array of stations in a narrow azimuth range) and synthetic seismograms is a powerful method for resolving the fine structure of the Earth's seismic velocities. For example, the D″ discontinuity (Lay & Helmberger 1983), an ultra-low velocity zone at the base of the mantle (Garnero *et al.* 1993), and the inner core transition zone (Song & Helmberger 1998) were all detected by such analyses. It is desirable to be able to use complete synthetic seismograms (which include all frequency components and all phases in the data) in studies of such regions, because we could then rigorously account for the effect of finite wavelength and the possibility of contamination by phases due to structure outside the region of interest. The methods presented in this paper allow complete synthetic seismograms to be computed up to, say, 2 Hz, without the need for ray-theoretical or earth-flattening approximations.

2 DIRECT SOLUTION METHOD FOR TI MEDIA

In this study we use the DSM (Geller & Ohminato 1994) to compute full-wave synthetics up to 2 Hz. The basic computational theory was published by Geller & Takeuchi (1995), hereafter cited as GT95, and Takeuchi *et al.* (1996), hereafter cited as TGC96, and the works cited therein. The above papers were limited to isotropic media, but the synthetics in this paper are extended to the case of TI media. This extension is relatively straightforward. However, in order to make accurate and efficient computations up to 2 Hz, several important technical problems had to be resolved. In particular, it is necessary to carefully and systematically determine the vertical grid spacing that must be used for various frequencies and angular orders. Failure to use a sufficiently fine grid can result in serious inaccuracy, while use of an overly fine grid will unnecessarily increase the CPU time. If the calculations are not cut off (i.e. if the grid for all angular orders always extends to the Earth's centre for P–SV calculations or to the CMB for SH calculations), the CPU time can be an order of magnitude larger than necessary. It thus is necessary to systematically determine the cut-off depth as a function of frequency and angular order.

As discussed below, the gridding problem and the cut-off depth problem are now well understood. The most recent publicly available versions of our codes (available for download at http://www-solid.eps.s.u-tokyo.ac.jp/∼dsm) now optimally handle these points. (We omit details, but earlier versions of our codes had problems.) The authors hope that these codes will be useful in a wide variety of seismological studies. We present sufficient details here so that users can understand the various trade-offs between accuracy and CPU time.

2.1 DSM—basic theory

In this paper, we first discuss the theory for extending optimally accurate DSM operators to TI media. Next we consider the problems caused by the evanescent regime (the region beneath the turning depth where the vertical component of the wavenumber vector is imaginary) and apply the error-estimation theory of GT95 to determine the grid spacing, maximum angular order and cut-off depth required to obtain accurate synthetics.

In this paper, subscripts r, θ, ϕ, denote vector components in locally Cartesian spherical coordinates. We use Greek subscripts and superscripts to denote components in the abstract vector space of trial functions. In this section, for the solid part of the medium these Greek indices correspond to a quadruplet of indices k, l, m and p for the index of the radial trial function, the angular order, the azimuthal order and the spherical harmonic component, respectively. In the fluid part of the medium the Greek indices correspond to a triplet of indices k, l, m, defined as above for the solid case. (See Geller & Ohminato 1994 and Cummins *et al.* 1997 for details.)

We use vector trial functions $\mathbf{\Phi}^{(\beta)}$ to represent the displacement in the solid part of the medium, and scalar trial functions $\Phi^{(\beta)}$ to represent the dependent variable, $Q = P/\omega$, where P is the change in the pressure, in the fluid part of the medium:

$$\begin{aligned} \boldsymbol{u} &= \sum_{\beta \in \text{solid}} c_\beta \mathbf{\Phi}^{(\beta)}, \\ Q &= \sum_{\beta \in \text{fluid}} c_\beta \Phi^{(\beta)}. \end{aligned} \tag{1}$$

As shown by Geller & Ohminato (1994), the DSM, as the name suggests, transforms the weak form of the elastic equation of motion to the following system of discretized linear equations, which are then directly solved:

$$(\omega^2 \mathbf{T} - \mathbf{H} + \omega \mathbf{R})\mathbf{c} = -\mathbf{g}, \tag{2}$$

where $\mathbf{T}$ is the mass (kinetic energy) matrix, $\mathbf{H}$ is the stiffness (potential energy) matrix, $\mathbf{g}$ is the excitation vector, and $\mathbf{R}$, which enforces continuity conditions at fluid–solid boundaries, is non-zero only for the spheroidal (P–SV) case.

The matrix elements and vector elements in eq. (2) are

$$\mathrm{T}_{\alpha\beta} = \begin{cases} \displaystyle\int_V \left(\Phi_i^{(\alpha)}\right)^* \rho \Phi_i^{(\beta)} \, dV & (\alpha, \beta) \in \text{solid} \\ \displaystyle\int_V (\Phi^{(\alpha)})^* \Phi^{(\beta)} / \lambda \, dV & (\alpha, \beta) \in \text{fluid} \\ 0 & \text{otherwise} \end{cases}, \tag{3}$$

$$\mathrm{H}_{\alpha\beta} = \begin{cases} \displaystyle\int_V \left(\Phi_{i,j}^{(\alpha)}\right)^* C_{ijkl} \Phi_{k,l}^{(\beta)} \, dV & (\alpha, \beta) \in \text{solid} \\ \displaystyle\int_V \left(\Phi_{,i}^{(\alpha)}\right)^* \Phi_{,i}^{(\beta)} / \rho \, dV & (\alpha, \beta) \in \text{fluid} \\ 0 & \text{otherwise} \end{cases}, \tag{4}$$

$$\mathrm{R}_{\alpha\beta} = \begin{cases} \int_S (\Phi^{(\alpha)})_i^* n_i^{(S)} \Phi^{(\beta)}\, dS & \alpha \in \text{solid and } \beta \in \text{fluid} \\ \int_S (\Phi^{(\alpha)})^* n_i^{(S)} \Phi_i^{(\beta)}\, dS & \alpha \in \text{fluid and } \beta \in \text{solid} \\ 0 & \text{otherwise,} \end{cases} \tag{5}$$

$$\mathrm{g}_\alpha = \begin{cases} \int_V \left(\Phi_i^{(\alpha)}\right)^* f_i\, dV & \alpha \in \text{solid} \\ -\int_V \left(\Phi_{,i}^{(\alpha)}\right)^* f_i/(\rho\omega)\, dV & \alpha \in \text{fluid} \end{cases}, \tag{6}$$

where * denotes complex conjugation, ρ is the density, C_{ijkl} is the elastic tensor in the solid, λ is the elastic modulus in the fluid, and $n_i^{(S)}$ is the outward unit normal to the solid regions at the fluid–solid boundaries. Anelastic attenuation is included in C_{ijkl} and λ, which are in general complex and frequency dependent. Note that the superscripts on the right-hand side of eqs (3)–(6) refer to the abstract vector space of trial functions, while the subscripts on the right-hand side of these equations refer to the physical space.

2.2 Transversely isotropic medium

Traveltime tomography for an isotropic model is greatly simplified because the group velocity, U, (which determines seismic traveltimes) is equal to the phase velocity, c, and neither depends on propagation direction. (This is of course the definition of isotropy.) On the other hand, both the group velocity and phase velocity for an anisotropic medium are functionals of the wavenumber $\boldsymbol{k}$; both depend on the propagation direction, and the two velocities are in general not equal (e.g. Helbig 1994). For a wave in Cartesian coordinates we have

$$p_x = \frac{k_x}{\omega},\ p_y = \frac{k_y}{\omega},\ p_z = \frac{k_z}{\omega}, \tag{7}$$

as the three components of the slowness vector and the components of the group velocity are given by

$$U_x = \frac{\partial\omega}{\partial k_x},\ U_y = \frac{\partial\omega}{\partial k_y},\ U_z = \frac{\partial\omega}{\partial k_z}. \tag{8}$$

Explicit expressions in spherical coordinates for the above quantities for a laterally homogeneous TI medium are given by Woodhouse (1981). The non-linearity of these expressions and their partial derivatives with respect to the elastic constants, and the dependence of the group velocity on propagation direction, means that inversion of traveltime data for the elastic constants of a global TI anisotropic model is considerably more difficult than inversion for an isotropic model. On the other hand, inversion of seismic waveform data is a promising approach for determining the Earth's anisotropic structure (e.g. Gung *et al.* 2003).

TI, the simplest anisotropy, is symmetric about the vertical axis. In spherical coordinates the constitutive equation is given by

$$\begin{pmatrix} \sigma_{\theta\theta} \\ \sigma_{\phi\phi} \\ \sigma_{rr} \\ \sigma_{\phi r} \\ \sigma_{r\theta} \\ \sigma_{\theta\phi} \end{pmatrix} = \begin{pmatrix} A & H & F & & & \\ H & A & F & & & \\ F & F & C & & & \\ & & & L & & \\ & & & & L & \\ & & & & & N \end{pmatrix} \begin{pmatrix} \varepsilon_{\theta\theta} \\ \varepsilon_{\phi\phi} \\ \varepsilon_{rr} \\ 2\varepsilon_{\phi r} \\ 2\varepsilon_{r\theta} \\ 2\varepsilon_{\theta\phi} \end{pmatrix}, \tag{9}$$

where σ and ε are the stress and strain tensors, respectively, the blank spaces in the matrix denote zeros, and A, C, F, L, N are the independent five elastic constants in TI, as defined by Love (1927). The dependent elastic constant H is given by

$$H = A - 2N. \tag{10}$$

In the isotropic case the elastic constants are as follows:

$$\begin{aligned} \lambda + 2\mu &= A = C \\ \mu &= L = N \\ \lambda &= F = H, \end{aligned} \tag{11}$$

where μ and λ are the Lamé constants.

2.3 Trial functions

All computations are carried out in spherical coordinates. The trial functions used in the expansions of the wavefield are given by eq. (1). Here we show the explicit form of the vector trial functions for the solid part of the medium. We use linear spline functions $X_k(r)$ for the vertically dependent part of the trial functions and vector spherical harmonics $\boldsymbol{S}_{lm}^1$, $\boldsymbol{S}_{lm}^2$ and $\boldsymbol{T}_{lm}$, defined as follows, for the laterally dependent part of the trial functions:

$$\begin{aligned} \boldsymbol{S}_{lm}^1(\theta,\phi) &= (Y_{lm}(\theta,\phi), 0, 0), \\ \boldsymbol{S}_{lm}^2(\theta,\phi) &= \left(0, \frac{1}{\mathcal{L}}\frac{\partial Y_{lm}(\theta,\phi)}{\partial\theta}, \frac{1}{\mathcal{L}\sin\theta}\frac{\partial Y_{lm}(\theta,\phi)}{\partial\phi}\right), \\ \boldsymbol{T}_{lm}(\theta,\phi) &= \left(0, \frac{1}{\mathcal{L}\sin\theta}\frac{\partial Y_{lm}(\theta,\phi)}{\partial\phi}, -\frac{1}{\mathcal{L}}\frac{\partial Y_{lm}(\theta,\phi)}{\partial\theta}\right), \end{aligned} \tag{12}$$

where $Y_{lm}\ (\theta,\phi)$ is a (fully normalized) surface spherical harmonic and $\mathcal{L} = \sqrt{l(l+1)}$. See (p. 181 Press *et al.* 1986) for a complete description of the spherical harmonics and associated Legendre polynomials.

The explicit form of the trial functions is as follows:

$$\begin{aligned} \boldsymbol{\Phi}^{(klm1)}(r,\theta,\phi) &= X_k(r)\boldsymbol{S}_{lm}^1(\theta,\phi), \\ \boldsymbol{\Phi}^{(klm2)}(r,\theta,\phi) &= X_k(r)\boldsymbol{S}_{lm}^2(\theta,\phi), \\ \boldsymbol{\Phi}^{(klm3)}(r,\theta,\phi) &= X_k(r)\boldsymbol{T}_{lm}(\theta,\phi). \end{aligned} \tag{13}$$

The scalar trial functions in the fluid regions are

$$\Phi^{(klm)}(r,\theta,\phi) = X_k(r)Y_{lm}(\theta,\phi). \tag{14}$$

We choose linear splines as the radially dependent part of the trial functions. Their explicit form is

$$X_k(r) = \begin{cases} (r - r_{k-1})/(r_k - r_{k-1}) & r_{k-1} < r \le r_k \\ (r_{k+1} - r)/(r_{k+1} - r_k) & r_k \le r < r_{k+1} \\ 0 & \text{otherwise} \end{cases}, \tag{15}$$

where $r_1 < r_2 \cdots < r_N$. The first and second lines of (eq. 15) are ignored for $k = 1$ and $k = N$, respectively.

2.4 Matrix elements

Due to the degeneracy of the spherically symmetric problem, the matrix elements depend only on l and are independent of m. The following discussion, therefore, considers the matrix elements and DSM equation of motion for some particular l and m; for simplicity we henceforth omit the indices l and m. We thus denote the elements of the matrices as $T_{k'p'kp}$ and $H_{k'p'kp}$ for the solid part of the medium, and $T_{k'k}$ and $H_{k'k}$ for the fluid part of the medium. $p = 1$ and $p = 2$ correspond to the spheroidal case, and $p = 3$ corresponds to the toroidal case.

We define the following intermediate integrals for the solid part of the medium:

$$I^0_{k'k} = \int dr \rho r^2 X_{k'} X_k \quad I^1_{k'k} = \int dr C r^2 \dot{X}_{k'} \dot{X}_k$$
$$I^2_{k'k} = \int dr L r^2 \dot{X}_{k'} \dot{X}_k \quad I^3_{k'k} = \int dr F r X_{k'} \dot{X}_k$$
$$I^4_{k'k} = \int dr L r \dot{X}_{k'} X_k \quad I^5_{k'k} = \int dr A X_{k'} X_k$$
$$I^6_{k'k} = \int dr L X_{k'} X_k \quad I^7_{k'k} = \int dr N X_{k'} X_k, \tag{16}$$

where the integrals (eq. 16) are non-zero only if $|k - k'| \leq 1$, ρ is the density and dots indicate differentiation with respect to r.

Using the above intermediate expressions, the matrix elements for the solid part of the medium for the spheroidal case ($p = 1$) or $p = 2$ are:

$$T_{k'1k1} = T_{k'2k2} = I^0_{k'k} ,$$
$$T_{k'1k2} = T_{k'2k1} = 0 , \tag{17}$$

and

$$H_{k'1k1} = I^1_{k'k} + 2\left(I^3_{k'k} + I^3_{kk'}\right) + 4I^5_{k'k} + \mathcal{L}^2 I^6_{k'k} - 4I^7_{k'k}$$
$$H_{k'2k2} = I^2_{k'k} - \left(I^4_{k'k} + I^4_{kk'}\right) + \mathcal{L}^2 I^5_{k'k} + I^6_{k'k} - 2I^7_{k'k}$$
$$H_{k'1k2} = -\mathcal{L}\left(I^3_{kk'} - I^4_{kk'} + 2I^5_{k'k} + I^6_{k'k} - 2I^7_{k'k}\right)$$
$$H_{k'2k1} = -\mathcal{L}\left(I^3_{k'k} - I^4_{k'k} + 2I^5_{k'k} + I^6_{k'k} - 2I^7_{k'k}\right) \tag{18}$$

The explicit form of the matrix elements for the toroidal case ($p = 3$) is:

$$T_{k'3k3} = I^0_{k'k} ,$$
$$H_{k'3k3} = I^2_{k'k} - I^4_{k'k} - I^4_{kk'} + I^6_{k'k} + (\mathcal{L}^2 - 2) I^7_{k'k}. \tag{19}$$

The integrals are taken from the CMB to the Earth' s surface or from the Earth's centre to the inner core boundary (ICB) for the respective solid regions. (We assume there is no ocean layer at the surface. If an ocean layer is present at the surface, it would be handled in the same way as the outer core.)

We define the following intermediate integrals for the fluid part of the medium:

$$I^{F0}_{k'k} = \int dr\ r^2 \dot{X}_{k'} \dot{X}_k / \lambda ,$$
$$I^{F1}_{k'k} = \int dr\ \dot{X}_{k'} \dot{X}_k / \rho ,$$
$$I^{F2}_{k'k} = \int dr\ r^2 \dot{X}_{k'} \dot{X}_k / \rho . \tag{20}$$

The matrix elements for the fluid part of the medium are

$$T_{k'k} = I^{F0}_{k'k}, \qquad H_{k'k} = \mathcal{L}^2 I^{F1}_{k'k} + I^{F2}_{k'k}. \tag{21}$$

At the boundary between the solid and fluid media, there are two nodes corresponding to the same depth. At the ICB the indices for these nodes are $k^-_{\rm ICB}$ for the solid medium and $k^+_{\rm ICB}$ for the fluid, while for the core mantle boundary (CMB) we have $k^-_{\rm CMB}$ for the fluid and $k^+_{\rm CMB}$ for the solid. As shown by (eqs 50 and 51 Geller & Ohminato 1994), **R** enforces the continuity of displacement and traction at fluid–solid boundaries. The only non-zero elements of **R** are:

$$R_{k^-_{\rm ICB}, k^+_{\rm ICB}} = R_{k^+_{\rm ICB}, k^-_{\rm ICB}} = r^2_{\rm ICB} ,$$
$$R_{k^-_{\rm CMB}, k^+_{\rm CMB}} = R_{k^+_{\rm CMB}, k^-_{\rm CMB}} = -r^2_{\rm CMB} , \tag{22}$$

where $r_{\rm ICB}$ and $r_{\rm CMB}$ are the radius at the ICB and CMB, respectively. The essential boundary condition $u_r = u_\theta = u_\phi = 0$ is imposed at $r = 0$.

2.5 Optimally accurate operators

The displacement in the previous section is represented using spherical harmonics for the lateral dependence and linear spline functions for the vertical dependence of the trial functions. The numerical operators derived using these trial functions are then replaced by optimally accurate operators (GT95; TGC96). Following TGC96, the submatrices in eq. (16) are replaced by the corresponding optimally accurate matrix operators. This can be done in a straightforward fashion, because the elastic moduli in eq. (16) of this paper are A, C, F, L, and N, while the elastic moduli in eq. (3) of TGC96 are λ and μ, but the functional forms of the various integrals in this paper are otherwise identical to those of TGC96. Similarly, the functional form of the toroidal integrals in eq. (19) is also identical to functional forms used in Cummins *et al.* (1994).

2.6 Excitation

In the vector spherical harmonics basis, the displacement can be written as

$$\boldsymbol{u}(r, \theta, \phi) = \sum_{lm} U_{lm}(r) \boldsymbol{S}^1_{lm} + V_{lm}(r) \boldsymbol{S}^2_{lm} + W_{lm}(r) \boldsymbol{T}_{lm}. \tag{23}$$

In terms of the trial functions used in this paper we can express $U_{lm}(r)$, $V_{lm}(r)$ and $W_{lm}(r)$ as follows:

$$U_{lm}(r) = \sum_k c_{klm1} X_k(r) ,$$
$$V_{lm}(r) = \sum_k c_{klm2} X_k(r) ,$$
$$W_{lm}(r) = \sum_k c_{klm3} X_k(r), \tag{24}$$

where the expansion coefficients give the value of U^m_l, V^m_l, and W^m_l at the nodes:

$$U^m_l(r_k) = c_{klm1},$$
$$V^m_l(r_k) = c_{klm2},$$
$$W^m_l(r_k) = c_{klm3}. \tag{25}$$

Hereafter in this section we drop the subscripts l and m on U, V, and W. The excitation is obtained from eq. (6). We consider the case of a point moment tensor on the z-axis ($r = r_s$, $\phi = 0$, $\theta \to 0$), for which the right-hand side of eq. (6) is zero except for $|m| \leq 2$. The excitation vector $\boldsymbol{g}$ can be determined by straightforward application of eq. (6). However, the body-force equivalents for certain moment tensor terms are kinematically equivalent to requiring $U(r)$, $V(r)$, or $W(r)$ to be discontinuous at the source depth (e.g. Takeuchi & Saito 1972, p. 290). This is an essential boundary condition (see Geller & Ohminato 1994, section 2) that will be violated by a straightforward application of eq. (6), thereby leading to suboptimal convergence. It is preferable to incorporate the displacement discontinuities directly into the definitions of $U(r)$, $V(r)$, and $W(r)$. The discontinuities are given by (p. 289 Takeuchi & Saito 1972).

$$D_1 = U(r)\big|^{r_s^+}_{r_s^-} = b_1 \delta_{m0} 2 M_{rr} \big/ \left(r_s^2 C_s\right)$$
$$D_2 = V(r)\big|^{r_s^+}_{r_s^-} = b_1 \delta_{m\pm1} (\mp M_{r\theta} + i M_{r\phi}) \big/ \left(r_s^2 L_s\right) ,$$
$$D_3 = W(r)\big|^{r_s^+}_{r_s^-} = b_1 \delta_{m\pm1} (i M_{r\theta} + \pm M_{r\phi}) \big/ \left(r_s^2 L_s\right), \tag{26}$$

where $C_s = C(r_s)$, $L_s = L(r_s)$ and $b_1 = \sqrt{(2l+1)/(16\pi)}$.

The remaining source terms involve discontinuities in the radial traction at the source depth, which is a natural boundary condition.

$$
\begin{aligned}
g_{k1} &= b_1\delta_{m0}2[M_{\theta\theta} + M_{\phi\phi} - 2M_{rr}F_s/C_s]X_k(r_s)/r_s \ , \\
g_{k2} &= b_1\delta_{m0}\mathcal{L}[-M_{\theta\theta} - M_{\phi\phi} + 2M_{rr}F_s/C_s]X_k(r_s)/r_s \ , \\
&\quad -b_2\delta_{m\pm2}(-M_{\theta\theta} + M_{\phi\phi} \pm i2M_{\theta\phi})X_k(r_s)/r_s \ , \\
g_{k3} &= b_2\delta_{m\pm2}(\mp iM_{\theta\theta} \pm iM_{\phi\phi} - 2M_{\theta\phi})X_k(r_s)/r_s
\end{aligned}
\tag{27}
$$

where $b_2 = \sqrt{(2l+1)(l-1)(l+2)/(64\pi)}$.

The above discussion applies to the case of a source exactly at a node. However, in most cases the source will be between nodes. For such cases we use the source representation of Takeuchi & Geller (2003), which allows us to calculate synthetics with the same accuracy as for a source at a node.

3 COMPUTATIONAL ISSUES

In this section, we first verify the accuracy of the synthetics, using solutions for deep focus earthquakes, and next compute synthetics for shallow earthquakes. Finally we consider ways in which the CPU time can be minimized without degrading the accuracy.

We compute three-component (vertical, radial and transverse) synthetic seismograms for the anisotropic (TI) PREM earth model (Dziewonski & Anderson 1981). (Anelastic attenuation is also included in the elastic constants using the above methods without using perturbation approximations.) As shown by Figs 1 and 2, the accuracy of the synthetic seismograms is improved by a factor of about 30 without increasing the CPU time by using optimally accurate numerical operators as opposed to conventional operators. This is the same order of improvement as was obtained by TGC96 for

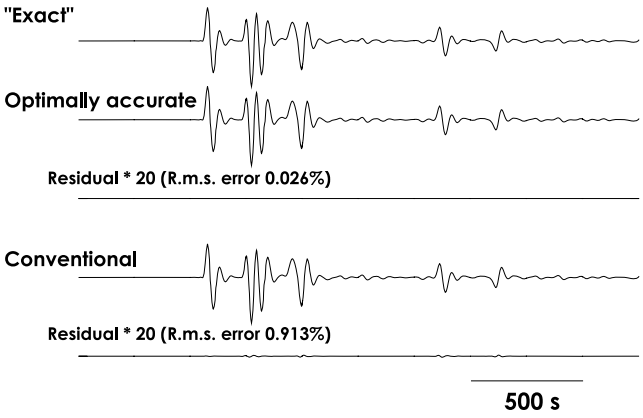

Figure 1. Toroidal (SH) velocity synthetic seismograms for the anisotropic PREM model (transverse component) computed up to 0.05 Hz and a maximum angular order of 2000 (about four times higher than required for practical calculations, to eliminate any possibility of errors due to truncation of the spherical harmonic expansion) using the source representation of Takeuchi & Geller (2003). The source is a 600-km-deep point double-couple source, with $M_{r\theta} = M_{\theta r} = 1$ and all other components of the moment tensor zero. The time dependence of the moment tensor for all of the calculations in this paper is a step-function. A low-pass six-pole filter with corners at 0.02 Hz is applied. The top trace is an essentially exact solution computed using the optimally accurate operators with 25 600 vertical intervals. The second and the fourth traces show the numerical solutions computed using optimally accurate (GT95; TGC96) and conventional numerical operators, respectively, with 3000 vertical intervals for each case. The third and fifth traces show the residuals for the second and fourth traces. The accuracy of the synthetics is improved by a factor about 30 by using optimally accurate operators without increasing the CPU time.

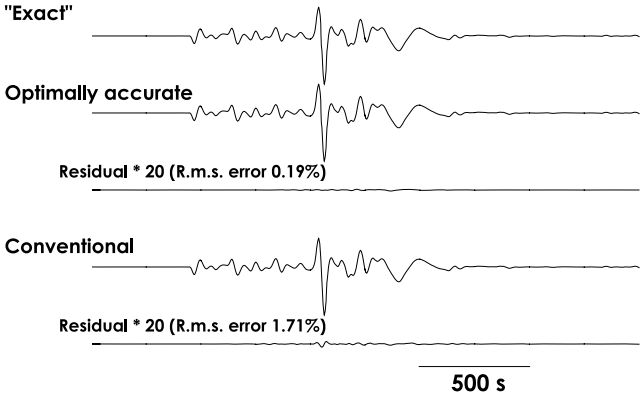

Figure 2. Spheroidal (P–SV) velocity synthetic seismograms for anisotropic PREM model (radial component) computed using the source representation of Takeuchi & Geller (2003). Details are the same as Fig. 1, except that 51 200 vertical intervals were used to compute the 'exact' trace and 6000 vertical intervals were used for the other traces. A larger number of vertical intervals (as compared to the toroidal case) is required than for Fig. 1, because the grid extends to the Earth's centre.

isotropic media. The synthetics in Figs 1 and 2 are calculated up to 0.05 Hz (20 s period) and a maximum angular order of 2000. The time dependence of the moment tensor for all of the calculations in this paper is a step-function. Note that the synthetics in Figs 1 and 2 are not the physical displacement components, as the toroidal and spheroidal wavefields have not yet been summed (see below). Although the examples in Figs 1 and 2 are relatively long-period synthetics, the ratio of performance improvement obtained by using the optimally accurate operators is independent of the frequency band. We, therefore, use only optimally accurate operators in the following computational examples.

The existence of anisotropy in the upper mantle affects long-period surface waves (Rayleigh and Love waves). For the anisotropic PREM structure, Rayleigh waves are slower and Love waves are faster than for isotropic PREM. To study the effects of anisotropic structure in the upper mantle, we calculated synthetic seismograms for anisotropic PREM, which includes TI structure between depths of 24.4 and 220 km. (Figs 3a and b). In these calculations the source is at a depth of 50 km, where TI structure exists in anisotropic PREM.

As a general rule of thumb if the gridding per wavelength is kept constant, the CPU time increases as the cube of the maximum frequency, because when the maximum frequency is doubled the number of frequencies, number of grid points, and maximum angular order all approximately double. Thus a calculation up to only 1 Hz requires only about one-eighth of the CPU time for a calculation up to 2 Hz for the same number of grids per vertical wavelength. In our calculations for Figs 1–6 we use a HPC, which has a Pentium 4, 3.2 GHz processor with the Intel Fortran Compiler (ifc). In our calculations for Figs 7–18, we use a HPC which has eight Pentium 4, 3.0 GHz processors with the Intel Fortran Compiler (IFC) using appropriate gridding for each angular order and a depth cut-off algorithm.

Synthetic seismograms must be computed with sufficient accuracy to allow comparison to observed data. The acceptable error must be determined by each user for each application, but the range between 1 per cent error and 0.1 per cent error is probably a typical requirement. We now consider the effect of the choice of vertical gridding and maximum angular order on the accuracy and CPU time of the synthetics. We begin by considering the relation between vertical gridding and accuracy (Fig. 4). To eliminate possible errors

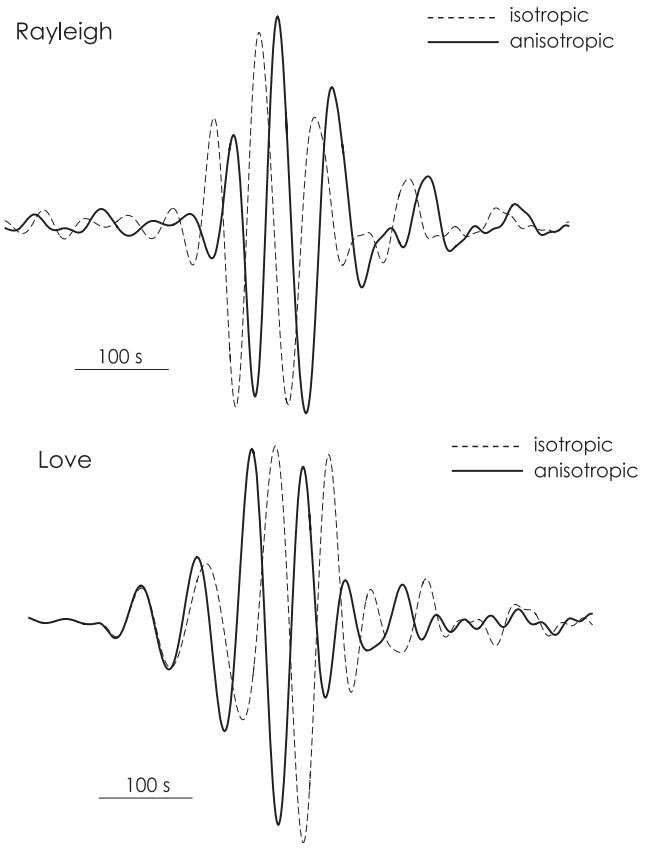

Figure 3. Synthetic seismograms (velocity, rather than displacement) for radial (top) and transverse (bottom) components for isotropic PREM and anisotropic PREM. A band-pass four-pole filter with corners at 0.01 and 0.02 Hz is applied. The source depth is 50 km and the epicentral distance is 70°. The anisotropic synthetics are delayed relative to the isotropic synthetics for Rayleigh waves, and advanced for Love waves, as expected for PREM.

due to truncation all calculations in Fig. 4 were carried out up to angular order 8000. The depth truncation and automatic angular order cut-off algorithms (see Fig. 6) were disabled for the calculations presented in Figs 4 and 5. Fig. 4 shows error and CPU time estimates for spheroidal synthetics for three passbands. For the passband up to 2 s period (0.5 Hz), a vertical grid with 6000 nodes gives an error of 1 per cent and a vertical grid with 16 000 nodes gives an error of about 0.1 per cent. The respective CPU times are about 12 000 and 34 000 s.

Next we consider the effect of maximum angular order on the solution error. Fig. 5 shows examples in which spheroidal expansions truncated at various angular orders are compared to a reference solution. All solutions used a vertical grid with 51 200 intervals to essentially eliminate errors due to vertical discretization. As shown in Fig. 5, truncation of the expansion at overly low angular orders leads to large errors, but once a critical threshold is passed the solution rapidly becomes highly accurate. Fig. 5 shows that the accuracy threshold for the initial *P*-wave is marginally lower than that for the complete synthetic, but that the difference is not significant.

We seek a physical interpretation of the angular order accuracy threshold. We denote the angular order where the drop in rms error occurs as l_d. Fig. 5 shows that l_d approximately depends on frequency, f (in Hz), as follows:

$$l_d \approx (7.5 \times 10^3 \text{ Hz}^{-1}) f. \tag{28}$$

The phase velocity is asymptotically given by:

$$c \approx \frac{\omega r}{l + \frac{1}{2}} = \frac{2\pi f r}{l + \frac{1}{2}}, \tag{29}$$

where r is the Earth's radius at the depth being considered. We obtain a phase velocity of about 5.2 km s^{-1} corresponding to l_d, which means that this is the slowest phase velocity component with significant amplitude in the high-frequency synthetics. Because the source is at a depth of 600 km, the excitation of high-frequency

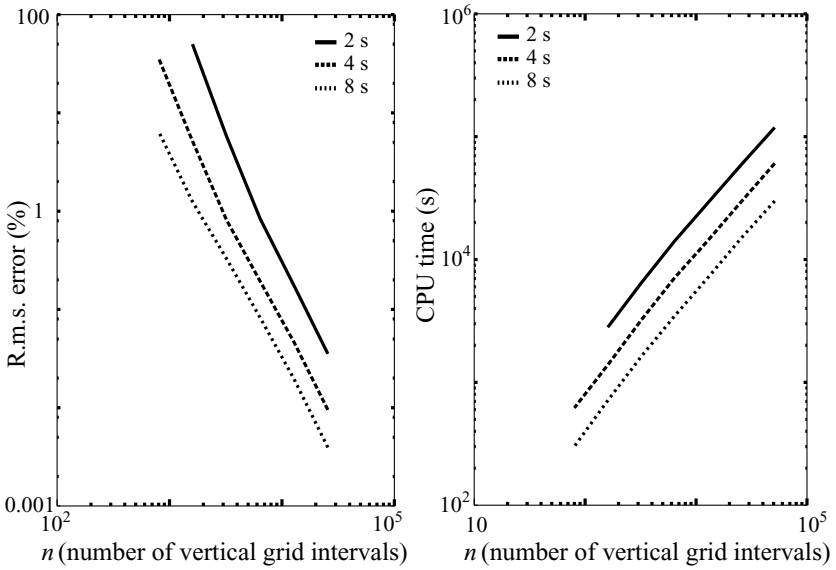

Figure 4. These figures show the dependence of rms error (left) and CPU time (right) on the number of vertical grid intervals, with the maximum angular order fixed to 8000. Synthetics were computed up to 8, 4 and 2 s (0.125, 0.25 and 0.5 Hz). The 'exact' synthetics used as the reference solution were computed using 51 200 vertical grid intervals, while the others were computed with fewer intervals.

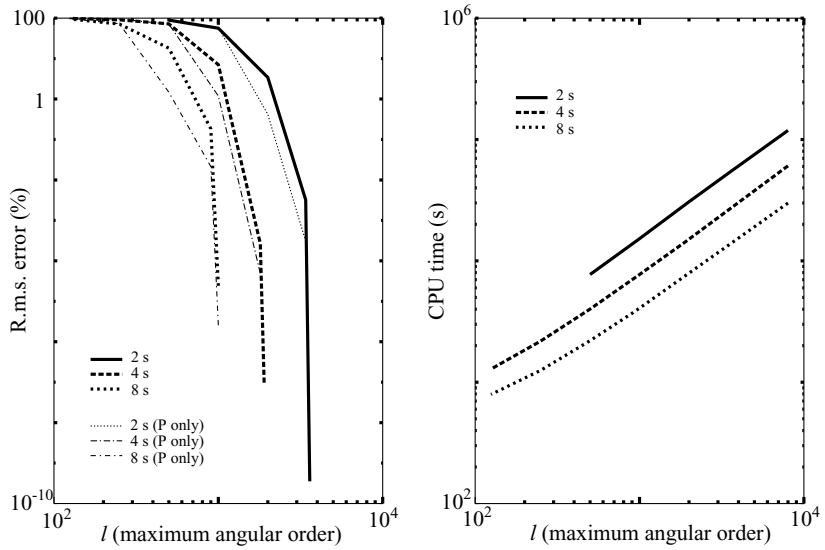

Figure 5. The dependence of rms error (left) and CPU time (right) on maximum angular order. The number of vertical grid intervals is fixed to 51 200. Variance reduction is shown for both the whole synthetic seismogram and also for only the portion including the initial *P* wave. Synthetics were computed for bands up to 8, 4 and 2 s (0.125, 0.25 and 0.5 Hz) using 51 200 vertical intervals. The 'exact' solutions for each band were computed including angular orders up to 8000.

Rayleigh and Love waves is essentially nil. In contrast, as discussed below, the accuracy threshold l_d for a shallow source is much higher than that shown in Fig. 5 or given by eq. (28).

The purpose of Figs 4 and 5 is to study the effect of grid spacing and maximum angular order on accuracy. However, in practical computations minimization of CPU time is also an important consideration. Our program uses an automatic angular order cut-off algorithm, so that unnecessary calculations are not made. In actual calculations our program solves eq. (2) for each angular order and frequency. Our program stops computing for a given frequency when the amplitude of the expansion coefficient decays beneath a user-specified fraction of the maximum amplitude for that frequency. In order to reduce the CPU time required to compute the matrix elements and to make the code simpler, our program only configures the vertical grid once, choosing a grid spacing which is sufficient for the worst case. As the angular order increases the turning depth (depth at which the wavefield's depth dependence changes from trigonometric to exponential) becomes steadily shallower. We use a depth cut-off algorithm (see below) to introduce a free surface boundary condition at an appropriate depth below the turning depth, thereby reducing the dimension of the matrix being solved in eq. (2). The above two cut-offs were disabled when producing Figs 4 and 5, but Fig. 6 shows that the CPU time is reduced by a factor of about 3.5 by using both the depth and angular order cut-offs. The depth and angular order cut-off are also used for shallow events (see below).

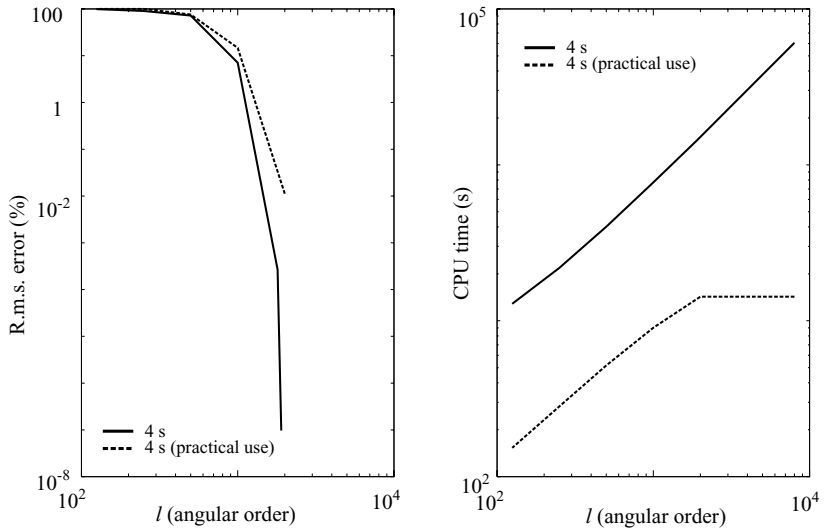

Figure 6. The dependence of rms error (left) and CPU time (right) on maximum angular order with (dashed line) and without (solid line) a depth cut-off and an angular order cut-off. Synthetics were computed for the band up to 4 s (0.25 Hz) with 51 200 vertical intervals (solid line) and with a grid spacing sufficiently small to yield a relative error of 10^{-2}, on the basis of eq. (31). These values were fixed in the calculation shown by the solid line but were reduced as appropriate by angular order and depth cut-off algorithms in the calculation shown by the dashed line. In the latter calculation the angular order cut-off was the lesser of the value on the horizontal axis and that given by eq. (28).

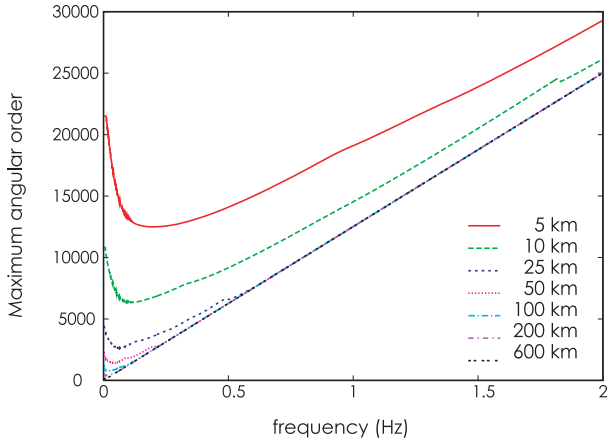

Figure 7. Maximum angular order required for computation of accurate spheroidal synthetic seismograms (for a receiver at the Earth's surface) at each frequency. The cut-off criteria is an amplitude of 10^{-5} of the maximum amplitude for that frequency. Accurate computation of synthetics for shallow earthquakes requires a larger maximum angular order for low frequencies, due to near-field terms. Also, for all frequencies synthetics for shallow events require computation up to higher angular orders than for deep focus earthquakes.

Fig. 7 raises important issues for workers who use modal superposition. For shallow sources (5 km depth) and low frequencies it is necessary to carry the spherical harmonic expansion to very high angular orders to obtain convergence. If modal summation were to be used it would be necessary to include modes up to this angular order in the summation (not necessarily only the fundamental mode, but also overtones, possibly to relatively high overtone number). The fundamental mode for $l = 20\,000$ has an eigenfrequency on the order of 1 Hz, and the overtones will have even higher frequencies. It is not obvious to what overtone number one would have to sum to obtain convergence for $l = 20\,000$ for the shallow event, but even if only the fundamental mode were needed this would mean having to sum modes whose eigenfrequency is on the order of 1 Hz to get accurate solutions for the displacement field at frequencies of, say, 0.01 Hz.

If the normal modes are a complete set then a summation of all of the modes will yield a complete synthetic seismogram. However, it appears to be widely believed (including by one reviewer of this paper) that complete synthetics up to some given frequency can be obtained by summing only those modes whose eigenfrequency is less than the specified frequency. Fig. 7 demonstrates that this belief is fallacious. Let us now consider the reasons.

In an anelastic model the frequency dependence of each mode is characterized by a resonance function, $(\omega^2 - \omega_m^2)^{-1}$. As Q becomes lower (i.e. as the imaginary part of ω_m becomes larger) the resonance peaks will become increasingly smeared out in frequency, so modes whose eigenfrequency is significantly higher than the frequency of interest can still make a non-negligible contribution, particularly if they interfere constructively, which is more likely to be the case when the source depth is near the receiver depth.

A careful study of the convergence of modal summation methods seems timely, and we hope that such a study will be conducted in the near future. Our guess is the correspondence between maximum frequency and maximum eigenfrequency will prove reasonable for the surface wave portion of the synthetics, especially at teleseismic distances, but will be found wanting for body waves, and may prove to be severely in error for the near-field part of the signal. In any case the DSM is solving a forced, rather than free, oscillation problem, so convergence is obtained as long as a sufficiently high angular order is used in the spherical harmonic expansion.

3.1 Synthetics for shallow events

The above examples are all for a deep (600 km) event. We now consider spheroidal synthetics for shallower events. For the case of deep earthquakes there is a more or less linear relation between the maximum angular order (i.e. the angular order that must be used as the upper limit in eq. 23 to obtain a sufficiently accurate synthetic) and the frequency. On the other hand, Fig. 7 shows that as the source depth becomes shallower, a linear relation (albeit with a higher maximum angular order) is still observed at high frequencies, but the maximum angular order also increases greatly at low frequencies. The reason for this behaviour is shown in Fig. 8. At a period of 100 s high angular order components of the wavefield (essentially near-field terms) with significant amplitudes exist in the vicinity of the source depth for both deep and shallow earthquakes. These terms contribute to the observable wavefield at the Earth's surface for shallow events, while for deep events they decay to a negligible value at the Earth's surface. Note, however, that if data from a deep earthquake were to be used in inversion for earth structure near the source depth, it might be necessary to use a much higher maximum angular order that is required for computing the wavefield at the Earth's surface, since the partial derivatives (Geller & Hara 1993)

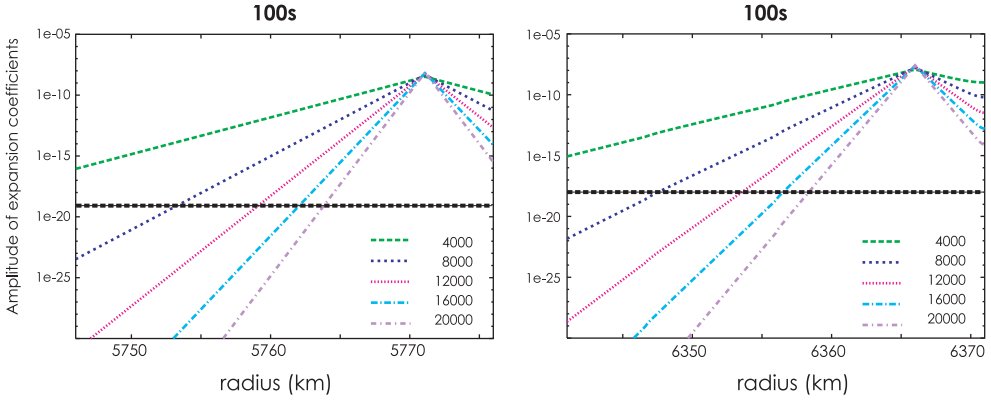

Figure 8. Decay of the amplitude of the depth-dependent part of the wavefield at a period of 100 s as a function of vertical distance from the source depth for (left) a source depth of 600 km and (right) a source depth of 5 km. The same basic behaviour is observed in both cases, but for the deep source the amplitude decays to a negligible value at the Earth's surface.

depend on the cross-correlation of the forward wavefield with the back-propagated wavefield at the location of the target.

3.2 Grid spacing and cut-off depth

As discussed above, the maximum angular order is one key parameter controlling the trade-off between accuracy and CPU time. However, in the calculations for any particular angular order, the two parameters that control the trade-off between accuracy and CPU time are the vertical grid spacing and the cut-off depth. We now discuss the considerations governing the choice of these parameters.

The appropriate values of the grid spacing and cut-off depth can be obtained using approximations based on familiar results for plane waves or cylindrical waves in an isotropic medium, as well as the well-known asymptotic relation (from eq. 29) between angular order and the horizontal component of the wavenumber vector:

$$k_x \approx \frac{l+\frac{1}{2}}{r}. \tag{30}$$

Our program automatically calculates the required grid spacing based on the desired relative error specified by the user. The relative error of the numerical solution is basically proportional to $|k_z^2 \Delta z^2|/12$ (see eq. 2.21 of GT95), where k_z is the vertical component of the wavenumber vector and Δz is the vertically grid spacing. The grid spacing required to produce a given relative error is thus approximately given by:

$$|\Delta z|^2 = \frac{12}{|k_z|^2} \times (\text{desired relative error}). \tag{31}$$

The vertical components of the wavenumbers for P and S waves are given, respectively, by:

$$k_{z\alpha}^2 = \frac{\omega^2}{\alpha^2} - k_x^2 \text{ and } k_{z\beta}^2 = \frac{\omega^2}{\beta^2} - k_x^2, \tag{32}$$

where

$$\alpha = \sqrt{\frac{\lambda+2\mu}{\rho}},\ \beta = \sqrt{\frac{\mu}{\rho}}. \tag{33}$$

When $k_z^2 > 0$ (i.e. when k_z is real) the vertical dependence of the wavefield is given by trigonometric functions whereas when $k_z^2 < 0$ it is given by exponential functions. The latter case is called the evanescent regime. The functional dependence is slightly more complicated for a spherical model, but is asymptotically the same.

The wavefield below the turning depth of body waves consists of evanescent waves. As the angular order l increases, the turning depth becomes progressively shallower. When the turning depth reaches the Earth's surface, then the wavefield at all depths will be in the evanescent regime. Even in cases where the source is located in the evanescent region (for some particular value of l) it is necessary to include such terms in the expansion (eq. 23) when they make a significant contribution to the numerical solution at depths of interest (usually, but not always, this will be the Earth's surface).

Fig. 8 shows that, although the amplitudes in the evanescent regime decay exponentially with increasing vertical distance from the source in either direction, the contribution of the evanescent terms at long periods can still be significant at the Earth's surface for shallow sources. This is the reason that the maximum angular order required for the shallowest source (shown in Fig. 7) increases with decreasing frequency. Truncating the spherical harmonic expansion at too low an angular order will result in inaccurate synthetics.

Because the amplitude of the solution below the turning depth decays exponentially (Fig. 9), it frequently will be unnecessary for the computational grid to extend to the Earth's centre for the spheroidal case or to the CMB for the toroidal case. In many cases we can cut off the computational grid by inserting a free surface boundary condition at an appropriate depth below the turning depth, which will significantly improve efficiency. We discuss the considerations governing the choice of the cut-off depth below.

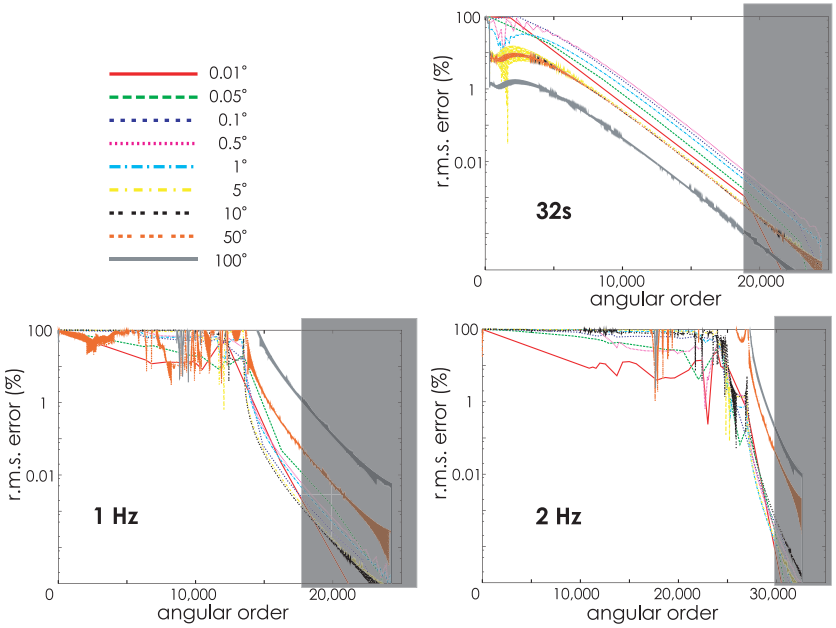

Figure 9. These figures show the contribution of the evanescent wave component to solution error. The rms errors were computed by comparing solutions truncated at the angular order shown on the horizontal axis to the 'exact' solution. The 'exact' solutions used as the reference were computed including up to angular orders 25 000 (for 32 s and 1 Hz) and 32 000 (for 2 Hz). The shaded regions indicate that the error estimates are somewhat questionable as the maximum angular order of the 'exact' solutions is approached. Note that even synthetics at teleseismic distances have substantial errors if the computation is truncated at too small an angular order.

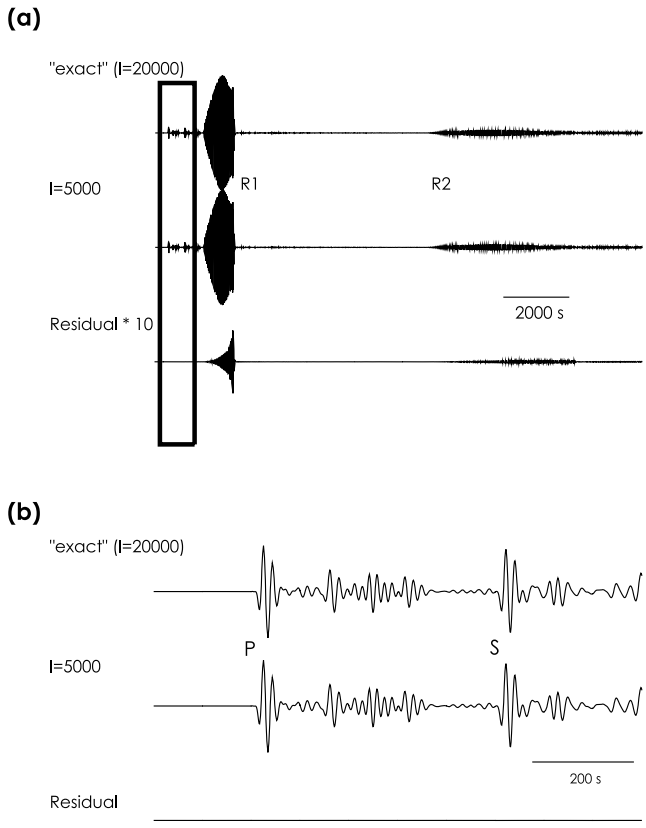

Figure 10. Examples of velocity synthetic seismograms (vertical component) for body and surface waves. The source is a 5-km-deep point double-couple source, with $M_{r\theta} = M_{\theta r} = 1$ and all other components of the moment tensor zero, and the epicentral distance is 60°. A low-pass four-pole filter with corners at 0.1 Hz is applied. (top) An essentially exact solution computed including angular orders up to 20 000; (middle) a solution computed including angular orders up to 5000; (bottom) the residual for the middle trace relative to the top trace. (b) An enlargement of the boxed region of (a) which includes the body wave arrivals.

In the travelling wave case k_z is at a maximum for $l = 0$ and decreases steadily as l increases until it reaches a value of 0 at the turning depth. $|k_z|$ will steadily increase with further increases in l, even though $k_z^2 < 0$. In many cases the largest value of $|k_z|$ will be the maximum value for the evanescent regime (at the maximum value of l used in the calculation) rather than the value for $l = 0$, and in such cases this will govern the choice of Δz.

We now present examples showing the contribution of the evanescent wave components to synthetics in the frequency and time domains. We consider a source 5 km below the Earth's surface and compute synthetics at the Earth's surface. When we compute synthetics for each frequency, we sum the solutions from $l = 0$ to the maximum angular order to obtain the synthetics. As the frequency increases, the convergence of the solution becomes more rapid once the evanescent regime is entered (Fig. 9).

Fig. 9 shows that regardless of the epicentral distance we have to compute synthetics up to a high angular order to accurately model the near-field terms. This will be generally true whenever spherical harmonics are used as the basis (i.e. for both the methods of this paper and modal superposition methods). From eq. (29) we find that for the 32 s case in Fig. 9, $c = 0.07\,\mathrm{km\,s^{-1}}$ for $l = 18\,000$. This suggests that using the phase velocity as the guide to when the expansion can be safely truncated is not an appropriate criterion when near-field terms contribute significantly to the solution.

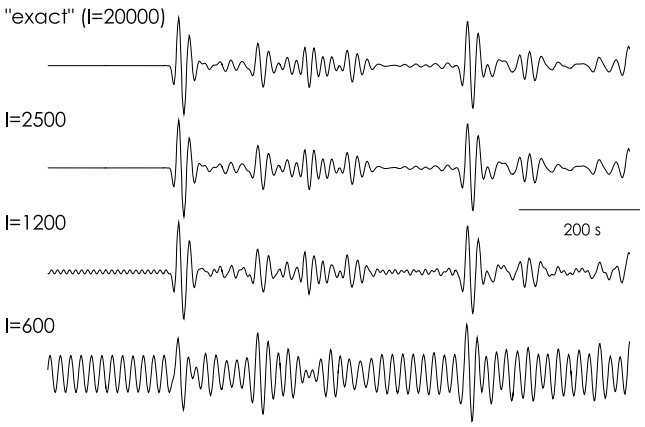

Figure 11. Examples of velocity synthetic seismograms (vertical component) for body and surface waves. The source is a 5-km-deep point double-couple source, with $M_{r\theta} = M_{\theta r} = 1$ and all other components of the moment tensor zero and the epicentral distance is 60°. A low-pass four-pole filter with corners at 0.1 Hz is applied. The top trace is an essentially exact solution computed including angular order up to 20 000. The second, third and fourth traces are computed using angular order up to 2500, 1200 and 600, respectively.

The far-field components of the solutions for high angular orders contribute to surface waves whose phase velocity is slow (Fig. 10 and eq. 29). If the synthetics are not computed up to a sufficiently high angular order, the surface waves in the synthetics will not be accurate.

Although it might appear that the error caused by truncation at too low an angular order will not significant affect body waves, this is not the case. Truncation at too low an angular order causes ringing because the truncation is essentially equivalent to employing a boxcar filter (Fig. 11). The effect of this error on the body waves will depend both on the time interval between the body waves and the surface waves and on the angular order at which the computation is truncated.

The amplitude of the vertically dependent part of the solution decays exponentially below the turning depth. As the angular order

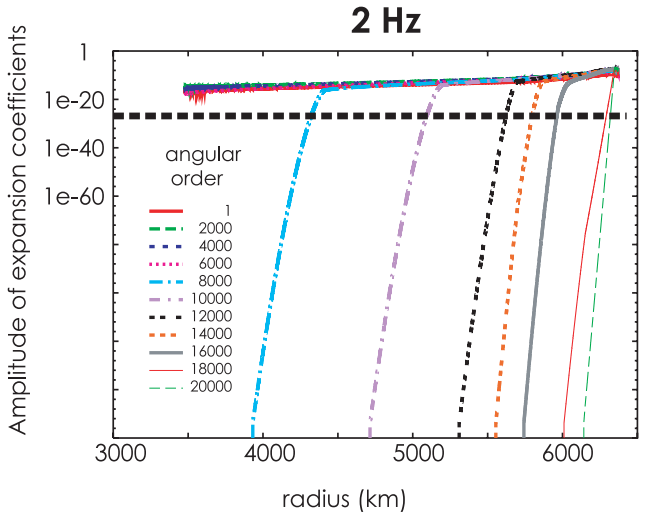

Figure 12. The amplitude of the expansion coefficients of toroidal displacement (the coefficient $W_{lm}(r)$ in eq. 23) as a function of depth for a source depth of 5 km. Solutions were computed for several angular orders. Horizontal line indicates the cut-off criterion (an amplitude of 10^{-10} of the maximum amplitude).

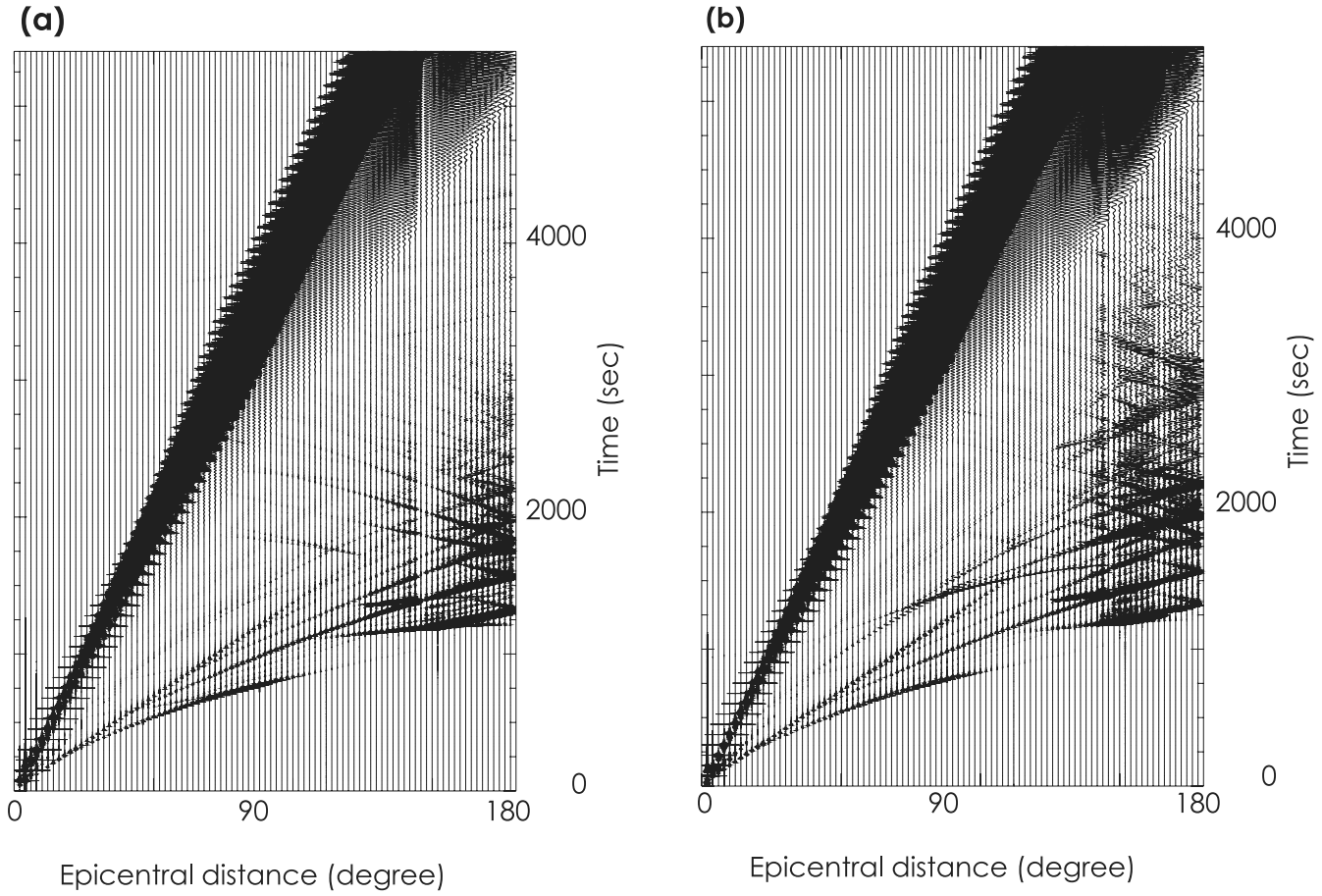

Figure 13. Three-component record section (velocity, rather than displacement) for the isotropic PREM model including anelastic attenuation and the sum of both the toroidal and spheroidal contributions to each horizontal component, with a maximum frequency of 2 Hz. The source is a 5-km-deep point double-couple source, with $M_{r\theta} = M_{\theta r} = 1$ and all other components of the moment tensor zero. (a) Vertical component; (b) radial component and (c) transverse component. All traces are unfiltered. Each trace is individually normalized to have the same maximum value. We can find sharp onsets of initial waves at teleseismic distance, reverberation phases and higher mode surface waves before the fundamental mode arrivals, which can be readily distinguished as the epicentral distance increases.

increases, the turning depth is shallower and the amplitude of the solutions decays more rapidly below the turning depth (Fig. 12). To reduce CPU time without significantly lessening the accuracy, we compute solutions only for the regions shallower than a cut-off depth, at which we impose a free-surface boundary condition. We choose the cut-off depth (Fig. 12) to be the depth below the turning depth at which the amplitude has decayed to 10^{-10} of the maximum amplitude. The use of a cut-off depth allows us to significantly reduce the CPU time without any appreciable loss in accuracy.

4 BROAD-BAND EXAMPLES: SYNTHETICS AND PROFILES

We compute three-component (vertical, radial, transverse) synthetic seismograms (Fig. 13) for the earth model, isotropic PREM (Dziewonski & Anderson 1981). (We used isotropic PREM for Fig. 13 so these results could be compared to calculations for other methods.) (Anelastic attenuation is also included.) We show record section synthetics computed up to 2 Hz. The CPU time required for the synthetics in Fig. 13 is about 3 months (12 weeks) using 8 processors. To compute synthetics up to 2 s, 2 weeks are required using our HPC. The detail of Figs 13, 14, 15, 16 and 18 can be clearly seen in the online version of the article.

The program uses the same grid for all frequencies. This makes the coding simpler and eliminates the need for computing matrix elements for several different grids, but means that the grid is finer than necessary for some frequencies. The maximum angular order will always occur at one of the endpoints of the period range because the dependence of maximum angular order on frequency is convex upward (Fig. 7). By examining the maximum angular order at both endpoints in advance of the computation we can thus determine the grid spacing required to achieve the required accuracy throughout the period range.

We now show several numerical examples to demonstrate the applicability of our methods to realistic problems. The waveforms of phases which sample several geodynamically interesting regions in the Earth are often complicated due to the presence of overlapping arrivals, which makes it hard to pick the arrival times. On the other hand, even for overlapping phases the waveform itself can be analysed by comparing synthetics and data For example, PKP branches sample the core well but their arrivals are very complicated (Fig. 14). As is well known, phases whose turning depths are in the mantle transition zone are also very complicated due to triplications caused by sharp velocity gradients (Fig. 15). For such complex but interesting regions, it may be advantageous to be able to directly analyse waveform data (e.g. either by waveform inversion

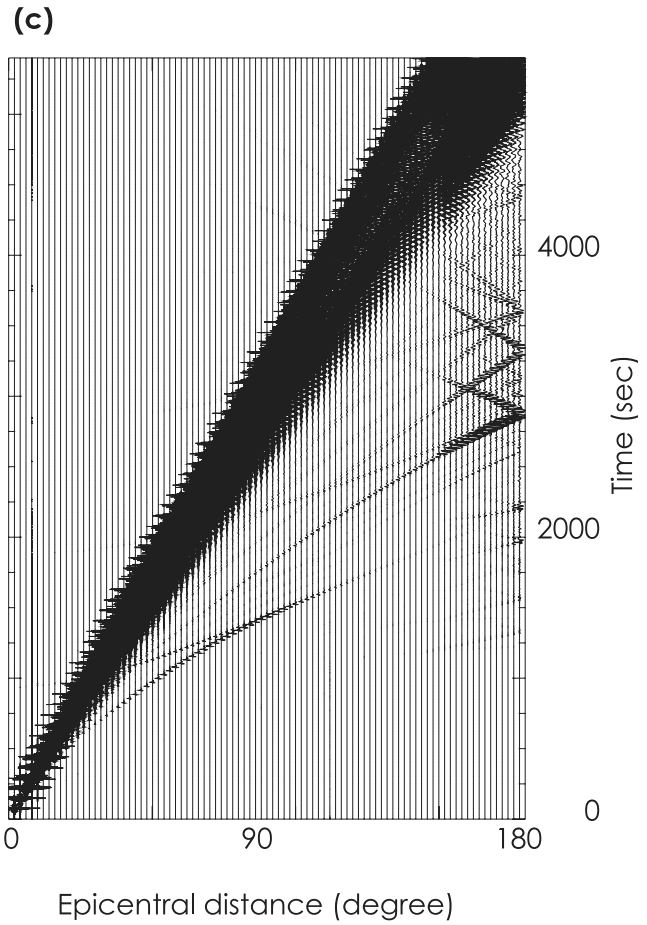

Figure 13 (*Continued*.)

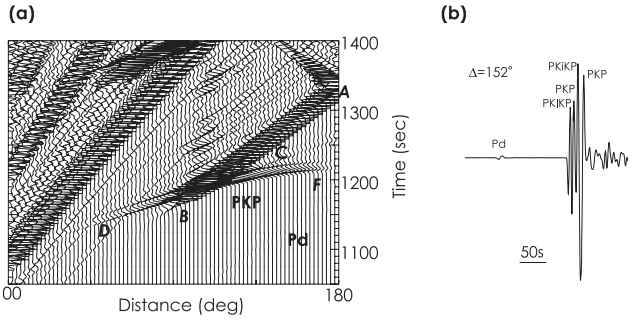

Figure 14. Examples of core phases (Pd and PKP) of synthetics. The source is a 5-km-deep point double-couple source, with $M_{r\theta} = M_{\theta r} = 1$ and all other components of the moment tensor zero. (a) Cross-section of core phases for epicentral distances between 100° and 180°; (b) synthetics of core phase for an epicentral distance of 152°.

or trial-and-error forward modelling) using the methods of this paper.

While it is well known that spheroidal and toroidal wavefields are coupled in the near field, spheroidal and toroidal wavefields are decoupled in the far field if asymptotic approximations are used. However, there in fact are spheroidal signals in the transverse component and toroidal signals in the radial component when calculations are made using the exact expressions for spherical harmonic functions rather than asymptotic approximations. As our method solves the elastic equation of motion for spherical coordinates without using

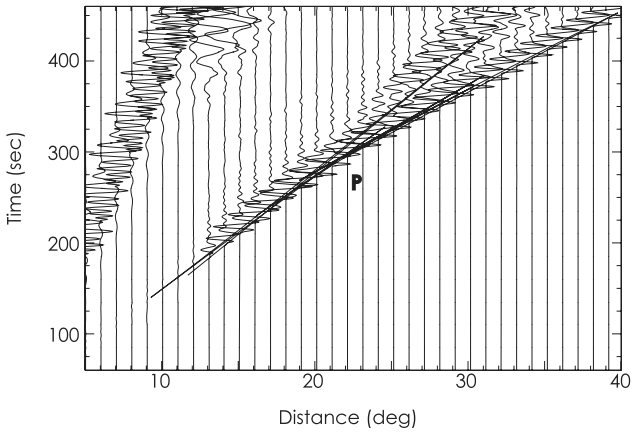

Figure 15. Examples of triplications in *P* waves sampling the transition zone for anisotropic PREM. The source is a 5 km deep point double-couple source, with $M_{r\theta} = M_{\theta r} = 1$ and all other components of the moment tensor zero. Traveltimes (computed independently) agree excellently with the synthetics.

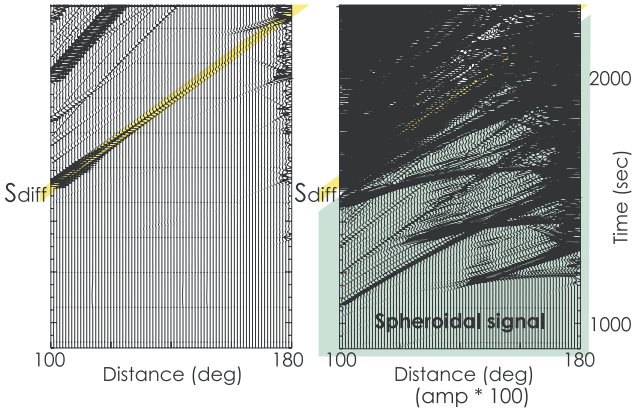

Figure 16. Record section for the transverse component just before and after the arrivals of Sd. The source is a 5-km-deep point double-couple source, with $M_{r\theta} = M_{\theta r} = 1$ and all other components of the moment tensor zero. Note that synthetics for the transverse component should include both toroidal and spheroidal contributions. The traces on the right are the same as those on the left but are amplified by a factor of 100 so that the spheroidal arrivals before Sd are clearly visible.

such approximations, we can accurately compute the spheroidal signals in the transverse component that arrive before the arrivals of diffracted *S* waves, which are the initial phase the in toroidal wavefield (Fig. 16).

Seismic waves propagating in the Earth are attenuated by intrinsic anelasticity. We showed above that essentially all the energy of waves for the far field is below 2 Hz for PREM. On the other hand, computations up to only 2 Hz are insufficient to fully calculate the near-field wavefield. Unfiltered synthetics up to 2 Hz for the near field, for an epicentral distance of 1°, show ringing and do not have a clear onset of the initial phase (Fig. 17a), while the unfiltered synthetics up to 2 Hz for the far field show a sharp onset (Fig. 17c). This indicates that near-field waves have significant energy in the frequency band higher than 2 Hz. If 'complete' ground motion synthetics for the near field are necessary, computation up to frequencies higher than 2 Hz is required. In many cases, it will be unnecessary to compute up to such high frequencies, and we can apply filters to the synthetics that simulate seismometers (Fig. 17b).

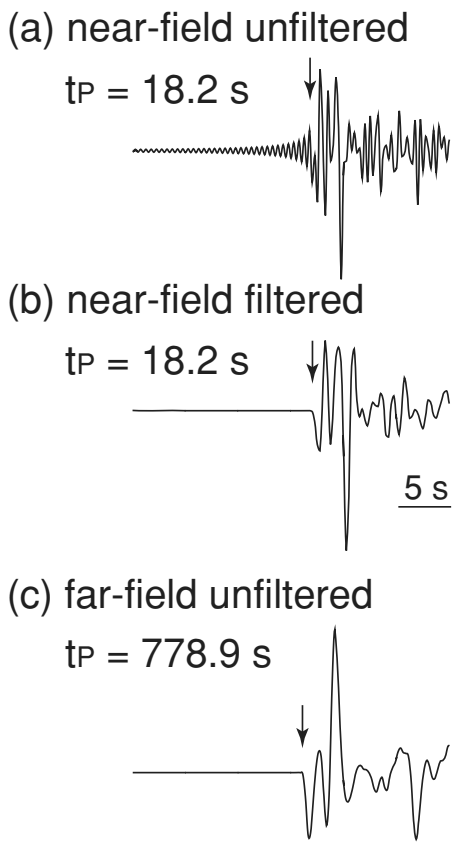

Figure 17. Examples of the initial phases of velocity synthetic seismograms (vertical component) for isotropic PREM for a point moment tensor source at a depth of 5 km with a δ-function source time function, with $M_{r\theta} = M_{\theta r} = 1$ and all other components of the moment tensor zero. (a) 2 Hz unfiltered synthetic for an epicentral distance of 1°, (b) synthetic for an epicentral distance of 1°, after applying a low-pass four-pole filter with a corner at 1 Hz and (c) 2 Hz unfiltered synthetic for an epicentral distance of 90°.

Note that synthetics in Fig. 17(c) are unfiltered. As a δ-function source time function is used, truncation of the calculation at a given frequency is equivalent to applying an acausal filter to the synthetics. This is why truncation at a frequency at which waves have a significant amplitude causes ringing (Fig. 17a). In order to obtain a sharp onset, we should calculate synthetics up to a sufficiently high frequency.

As discussed in the previous section, for the TI laterally homogeneous case we decompose eq. (2) into separate systems for each angular order. We then further decompose these systems into separate sets of linear equations for the toroidal (*SH*) and spheroidal (*P–SV*) displacement. After these displacement fields are separately computed, we then sum them to obtain the synthetics. As shown by eq. (12), both the spheroidal and toroidal wavefields have non-zero θ- and ϕ-components, so it is necessary to sum both to obtain accurate synthetics for the horizontal components of displacement (Fig. 18).

If we look at only the spheroidal or toroidal wavefields we find non-physical waves that have apparent velocity, which is infinite (Fig. 18: left and centre). These non-physical waves vanish when both spheroidal and toroidal contributions are summed (Fig. 18: right). Although the properties of the non-physical waves are not fully understood, the important point is that these artefacts are eliminated by summing the toroidal and spheroidal contributions to the horizontal displacement.

5 DISCUSSION

The methods presented in this paper can also be used in waveform inversion calculations for 1-D and 3-D earth models (Geller & Hara 1993). To invert for 3-D structure we would treat the laterally heterogeneous part of the structure as a perturbation to the laterally homogeneous part of the model and use the Born expansion (Takeuchi *et al.* 2000; Igel *et al.* 2000). If we use only the first-term (the first-order Born expansion) accuracy is limited, but by taking the expansion to third or fourth order, accuracy can be greatly improved. Note that the details of how to apply the DSM to laterally heterogeneous models are thoroughly discussed by Cummins *et al.* (1997) for the isotropic case, and their methods can also be used for the anisotropic case.

ACKNOWLEDGMENTS

We thank Daisuke Suetsugu and Tatsuhiko Hara for critically reading the manuscript. This research was partly supported by grants from the Japanese Ministry of Education, Science and Culture

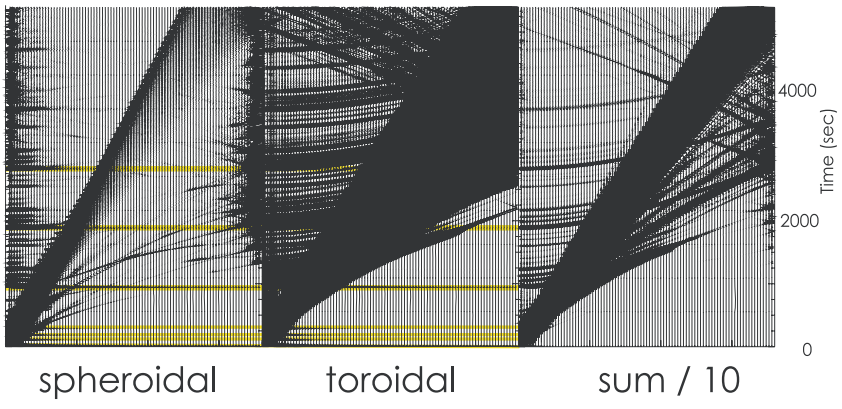

Figure 18. ϕ-component (transverse component) record sections (velocity, rather than displacement) for isotropic PREM model including anelastic attenuation. The source is a 5-km-deep point double-couple source, with $M_{r\theta} = M_{\theta r} = 1$ and all other components of the moment tensor zero. (left) Spheroidal contribution; (centre) toroidal contribution; (right) one-tenth of the sum of the spheroidal and toroidal contributions (scaled down in order to prevent the amplitude from being saturated). Non-physical waves can be seen in the left and centre record sections. as shown by the yellow lines. These non-physical waves are eliminated when we sum the spheroidal and toroidal components. Non-physical waves are not found in the vertical component of spheroidal synthetics.

(Nos. 17037001 and 17540392). KK was supported by a JSPS Fellowship for Young Scientists.

REFERENCES

Ascher, U., 1988. Hybrid methods in reflectivity calculations, in *Seismological Algorithms, Computational Methods and Computer Programs*, pp. 321–370, ed. Doornbos, D.J., Academic Press, London.

Chapman, C.H. & Phinney, R.A., 1970. Diffraction of P waves by core and an inhomogeneous mantle, *Geophys. J. R. astr. Soc.,* **21,** 185–202.

Cummins, P.R., Geller, R.J., Hatori, T. & Takeuchi, N., 1994. DSM complete synthetic seismograms: SH, spherically symmetric, case, *Geophys. Res. Lett.,* **21,** 533–536.

Cummins, P.R., Takeuchi, N. & Geller, R.J., 1997. Computation of complete synthetic seismograms for laterally heterogeneous models using the Direct Solution Method, *Geophys. J. Int.,* **130,** 1–16.

Dziewonski, A.M. & Anderson, D.L., 1981. Preliminary reference Earth model, *Phys. Earth planet. Inter.,* **25,** 297–356.

Fryer, G.J. & Frazer, L.N., 1987. Seismic waves in stratified anisotropic media—II. Elastodynamic eigensolutions for some anisotropic systems, *Geophys. J. R. astr. Soc.,* **91,** 73–101.

Friederich, W. & Dalkolmo, J., 1995. Complete synthetic seismograms for a spherically symmetric earth by a numerical computation of the Green's function in the frequency domain, *Geophys. J. R. astr. Soc.,* **122,** 537–550.

Garnero, E.J. & Lay, T., 2003. D″ shear velocity heterogeneity, anisotropy and discontinuity structure beneath the Carribean and Central America, *Phys. Earth planet. Inter.,* **140,** 219–242.

Garnero, E.J., Grand, S.P. & Helmberger, D.V., 1993. Low P-wave velocity at the base of the mantle, *Geophys. Res. Lett.,* **20,** 1843–1846.

Geller, R.J. & Hara, T., 1993. Two efficient algorithms for iterative linearized inversion of seismic waveform data, *Geophys. J. Int.,* **115,** 699–710.

Geller, R.J. & Ohminato, T., 1994. Computation of synthetic seismograms and their partial derivatives for heterogeneous media with arbitrary natural boundary conditions using the Direct Solution Method, *Geophys. J. Int.,* **116,** 421–446.

Geller, R.J. & Takeuchi, N., 1995. A new method for computing highly accurate DSM synthetic seismograms, *Geophys. J. Int.,* **123,** 449–470.

Gilbert F., 1971. Excitation of normal modes of the Earth by earthquake source, *Geophys. J. R. astr. Soc.,* **22,** 223–226.

Gung, Y., Panning, M. & Romanowicz, B., 2003. Global anisotropy and the thickness of continents, *Nature,* **422,** 707–711.

Helbig, K., 1994. *Foundations of Anisotropy for Exploration Seismics*, Pergamon, Oxford.

Helmberger, D.V., 1974. Generalized ray theory for shear dislocations, *Bull. seism. Soc. Am.,* **64,** 45–64.

Igel, H., Takeuchi, N., Geller, R.J., Megnin, C., Bunge H.-P., Clévédé, E., Dalkolmo J. & Romanowicz B., 2000. The COSY Project: verification of global seismic modeling algorithms, *Phys. Earth planet. Inter.,* **119,** 3–23.

Karato, S., 1998. Some remarks on the origin of seismic anisotropy in the D″ layer, *Earth Planets Space,* **50,** 1019–1028.

Keith, C.M. & Crampin, S., 1977. Seismic body waves in anisotropic media: propagation through a layer, *Geophys. J. R. astr. Soc.,* **49,** 209–223.

Kendall, J-M. & Nangini, C., 1996. Lateral variations in D″ below the Caribbean, *Geophys. Res. Lett,* **23,** 399–402.

Kennett, B.L.N., 1988. Systematic approximations to the seismic wavefield, in *Seismological Algorithms, Computational Methods and Computer Programs*, pp. 237–259, ed. Doornbos, D.J., Academic Press, London.

Lay, T. & Helmberger, D.V., 1983. A lower mantle *S*-wave triplication and the shear velocity structure of D″, *Geophys. J. R. astr. Soc.,* **75,** 799–837.

Li, X.-D. & Romanowicz, B., 1995. Comparison of global waveform inversions with and without considering cross-branch modal coupling, *Geophys. J. Int.,* **121,** 695–709.

Love, A.E.H., 1927. *A Treatise on the Mathematical Theory of Elasticity*, Cambridge University Press, Cambridge.

Mitchell, B.J. & Helmberger, D.V., 1973. Shear velocities at the base of the mantle from observations of *S* and *ScS*, *J. geophys. Res.,* **78,** 6009–6020.

Montagner, J.-P. & Kennett, B.L.N., 1996. How to reconcile body-wave and normal-mode reference earth models, *Geophys. J. Int.,* **125,** 229–248.

Moore, M.M., Garnero, E.J., Lay, T. & Williams, Q., 2004. Shear wave splitting and waveform complexity for lowermost mantle structures with low-velocity lamellae and transverse isotropy, *J. geophys. Res.,* **109,** doi:10.1029/2003JB002546.

Park, J., 1997. Free oscillations in an anisotropic earth: path-integral asymptotics, *Geophys. J. Int.,* **129,** 399–411.

Press, W.H., Flannery, S.A., Teukolsky, S.A. & Vetterling, W.T., 1986. *Numerical Recipes*, Cambridge University Press, Cambridge.

Rost, S. & Garnero, E., 2004. Array seismology advances Earth interior research, *EOS, Trans. Am. geophys. Un.,* **85,** 301, 305–306.

Rost, S. & Thomas, C., 2002. Array seismology: Methods and applications, *Rev. Geophys.,* **40,** doi:10.1029/2000RG000100.

Shito, A. & Shibutani, T., 2001. Upper mantle transition zone structrure beneath the Philippine Sea Region, *Geophys. Res. Lett.,* **28,** 871–874.

Song, X.D. & Helmberger, D.V., 1998. Seismic evidence for an inner core transition zone, *Science,* **282,** 924–927.

Suetsugu, D., Shinohara, M., Araki, E., Kanazawa, T., Suyehiro, K., Yamada, T., Nakahigashi, K., Shiobara, H., Sugioka, H., Kawai, K. & Fukao, Y., 2005. Mantle discontinuity depths beneath the West Philippine Basin from receiver function analysis of deep-sea borehole and seafloor broadband waveforms, *Bull. seism. Soc. Am.,* **95,** 1947–1956.

Sutherland, F.H., Vernon, F.L., Orcutt, J.A., Collins, J.A. & Stephen, R.A., 2004. Results from OSNPE: improved teleseismic earthquake detection at the seafloor, *Bull. seism. Soc. Am.,* **94,** 1868–1878.

Tajima, F. & Grand, S.P., 1998. Variation of transition zone high-velocity anomalies and depression of 600 km discontinuity associated with subduction zones from the southern Kuries to Izu-Bonin and Ryukyu, *J. geophys. Res.,* **103,** 15 015–15 036.

Takeuchi, H. & Saito, M., 1972. Seismic surface waves, *Meth. comp. Phys.,* **11,** 217–295.

Takeuchi, N. & Geller, R.J., 2003. Accurate numerical methods for solving the elastic equation of motion for arbitrary source locations, *Geophys. J. Int.,* **154,** 852–866.

Takeuchi, N., Geller, R.J. & Cummins, P.R., 1996. Highly accurate P-SV complete synthetic seismograms using modified DSM operators, *Geophys. Res. Lett.,* **23,** 1175–1178.

Takeuchi, N., Geller, R.J. & Cummins, P.R., 2000. Complete synthetic seismograms for 3-D heterogeneous Earth models computed using modified DSM operators and their applicability to inversion for Earth structure, *Phys. Earth planet. Inter.,* **119,** 25–36.

Tseng, T.-L. & Chen, W.-P., 2004. Contrasts in seismic wave speeds and density across the 660-km discontinuity beneath the Philippine and the Japan Seas, *J. geophys. Res.,* **109,** doi:10.1029/2003JB002613.

Woodhouse, J.H., 1981. A note on the calculation of traveltimes in a transversely isotropic Earth model, *Phys. Earth planet. Inter.,* **25,** 357–359.

Woodhouse, J.H., 1988. The calculation of eigenfrequencies and eigenfunctions of the free oscillations of the Earth and the Sun, in *Seismological Algorithms, Computational Methods and Computer Programs*, pp. 321–370, ed. Doornbos, D.J., Academic Press, London.

Woodhouse, J.H. & Dziewonski, A.M., 1984. Mapping the upper mantle: three-dimensional modeling of Earth structure by inversion of seismic waveforms, *J. geophys. Res.,* **89,** 5953–5986.

Young, C.J. & Lay, T., 1990. Multiple phase analysis of the shear velocity structure in the D″ region beneath Alaska, *J. geophys. Res.,* **95,** 17 385–17 402.

Yu, Y. & Park, J., 1993. Upper mantle anisotropy and coupled-mode long-period surface waves, *Geophys. J. Int.,* **114,** 473–489.